Journal of Solid State Chemistry 184 (2011) 921–928

Contents lists available at ScienceDirect

Journal of Solid State Chemistry

journal homepage: www.elsevier.com/locate/jssc

Structural, optoelectronic, infrared and Raman spectra of orthorhombic $SrSnO_3$ from DFT calculations

E. Moreira [a], J.M. Henriques [b], D.L. Azevedo [c,a], E.W.S. Caetano [d,*], V.N. Freire [e], E.L. Albuquerque [f]

[a] Departamento de Física Teórica e Experimental, Universidade Federal do Rio Grande do Norte, 59072-970 Natal-RN, Brazil
[b] Centro de Educação e Saúde, Universidade Federal de Campina Grande, Campus Cuité, 58175-000 Cuité-PB, Brazil
[c] Departamento de Física, Universidade Federal do Maranhão, Centro de Ciências Exatas e Tecnologia, 65085-580 São Luís-MA, Brazil
[d] Instituto Federal de Educação, Ciência e Tecnologia do Ceará, Av. 13 de Maio, 2081, Benfica, 60040-531 Fortaleza-CE, Brazil
[e] Departamento de Física, Universidade Federal do Ceará, Centro de Ciências, Caixa Postal 6030, Campus do Pici, 60455-760 Fortaleza-CE, Brazil
[f] Departamento de Biofísica e Farmacologia, Universidade Federal do Rio Grande do Norte, 59072-970 Natal-RN, Brazil

ARTICLE INFO

Article history:
Received 24 November 2010
Received in revised form
21 January 2011
Accepted 11 February 2011
Available online 19 February 2011

Keywords:
Orthorhombic $SrSnO_3$
Structural properties
Band structure
Effective masses
Optical properties

ABSTRACT

Orthorhombic $SrSnO_3$ was investigated using density functional theory (DFT) considering both the local density and generalized gradient approximations, LDA and GGA, respectively. The electronic band structure, density of states, complex dielectric function, optical absorption, and the infrared and Raman spectra were computed. Calculated lattice parameters are close to the experimental measurements, and an indirect band gap $E(S\rightarrow\Gamma)=1.97$ eV (2.27 eV) was obtained within the GGA (LDA) level of calculation. Effective masses for holes and electrons were estimated, being very anisotropic in comparison with similar results for orthorhombic $CaSnO_3$. The complex dielectric function and the optical absorption of $SrSnO_3$ were shown to be sensitive to the plane of polarization of the incident light. The infrared spectrum between 100 and 600 cm^{-1} was obtained, with its main peaks being assigned, and a nice agreement between experimental and theoretical peaks of the Raman spectrum of orthorhombic $SrSnO_3$ was achieved.

1. Introduction

Alkaline earth stannates, $A\ SnO_3$ (A=Ba, Sr and Ca), attract technological interest due to their applications as transparent conducting oxides (TCOs), which are employed in the fabrication of transparent electrodes for photovoltaic cells and organic light-emitting diodes [1–6]. $A\ SnO_3$ materials also have been used to develop new chemical sensors [7], stable capacitors [8], water photoelectrolysis systems [9,10], antistatic coatings [11] and flat panel displays [12]. $CaSnO_3$ and $SrSnO_3$ are also used in lithium batteries and humidity sensors [13]. Perovskite-type transparent and conductive oxide films of $SrSnO_3$ doped with Sb were successfully grown on $SrTiO_3$(001) substrates using a pulsed laser deposition method [14], exhibiting good transmittance in the visible spectrum and electrical conductivity at room temperature.

Taking into account the technological and theoretical interest in the ABO_3 perovskite materials, we have previously performed computational simulations within the density functional theory (DFT) framework, using both local density and generalized gradient approximations (LDA and GGA, respectively) of the structural, electronic, and optical properties for orthorhombic $CaGeO_3$ [15], $CaSnO_3$ [16], $CaPbO_3$ [17] and $CdX\ O_3$ (X=C, Si, Ge, Sn, Pb) [18]. The calculated band structures suggest an indirect band gap ($S\rightarrow\Gamma$) for $CaGeO_3$ ($\approx$2.3 eV), and a direct band gap for $CaSnO_3$ ($\approx$2.9 eV) and $CaPbO_3$ ($\approx$0.94 eV). For a set of $CdX\ O_3$ crystals (X=C, Si, Ge, Sn, Pb), our simulations predict indirect band gaps for the hexagonal $CdCO_3$ and triclinic $CdSiO_3$ crystals, and direct band gaps for orthorhombic $CdGeO_3$ and $CdSnO_3$. Calcium stannate ($CaSnO_3$), on the other hand, presents two crystalline forms: an ilmenite phase with rhombohedral unit cell [19], and an orthorhombic phase with perovskite structure [20]. Two studies on the electronic structure study of $CaSnO_3$ ilmenite [21] and $CaSnO_3$ orthorhombic [12] were carried out using the Perdew–Wang generalized gradient approximation (GGA) exchange-correlation functional, predicting band gaps of 4.0 eV for ilmenite $CaSnO_3$ (experimental value 4.4 eV), and 2.9 eV for orthorhombic $CaSnO_3$.

Calculations performed within the full-potential linearized augmented plane wave (FLAPW) method and using the local spin density approximation (LSDA) for the exchange-correlation energy, predicted that perovskite strontium stannate ($SrSnO_3$) is a semiconductor with an indirect band gap (R and $M\rightarrow\Gamma$) of $\approx$1.03 eV [22]. Bannikov et al. [23], using the FLAPW approach with a GGA exchange-correlation functional, have studied the

* Corresponding author. Fax: +55 85 3307 3711.
E-mail address: ewcaetano@gmail.com (E.W.S. Caetano).

0022-4596/$ - see front matter © 2011 Elsevier Inc. All rights reserved.
doi:10.1016/j.jssc.2011.02.009

electronic and magnetic properties of non-magnetic cubic SrM O_3 (M=Ti, Zr and Sn) perovskites and found a direct band gap of 0.95 eV for the cubic phase of $SrSnO_3$ [23]. Band structure calculations within the DFT-GGA approximation, UV-visible diffuse reflectance, and photoluminescence spectroscopy were used to study the emission mechanism of orthorhombic $SrSnO_3$ [9], the calculated band gap for orthorhombic $SrSnO_3$ being 1.8 eV. Experimental measurements of ultraviolet diffuse reflectance and computational studies on the electronic structure of ternary oxides performed using linear muffin-tin orbital (LMTO) method obtained an experimental energy band gap of 4.1 eV and a calculated energy band gap of 2.5 eV for orthorhombic $SrSnO_3$ [12].

X-ray measurements revealed that $SrSnO_3$ can assume cubic [24,25] and orthorhombic [26] crystal structures (the last one with spacial group *Pbnm*). Glerup et al. reported the existence of three structural phase transitions in $SrSnO_3$, approximately at 900, 1070 and 1300 K [27]. $SrSnO_3$ crystalline phases with space groups *Pmcn*, *Incn*, *I*4/*mcm* were observed by the same authors at temperatures of 573, 973 and 1173 K, respectively. The cubic structure *Pm*3*m* has been identified at 1295 K, while in the temperature range between 298 and 905 K, $SrSnO_3$ crystals are orthorhombic.

It is the aim of this work to present the structural and optoelectronic properties of orthorhombic strontium stannate $SrSnO_3$ within the scope of the density functional theory (DFT) formalism using two approximations for the exchange-correlation functional: the local density approximation (LDA) and generalized gradient approximation (GGA). During the analysis of the data we obtained, we will eventually make comparisons with previous results for orthorhombic $CaSnO_3$ in order to understand the effect of replacing Ca with Sr. The electronic band structure, electronic densities of states, band gaps, effective masses, and optical properties (dielectric function and absorption) will be presented, together with the calculated infrared and Raman spectra (the last one being compared with experimental results [28,29]), dielectric permittivity and polarisability tensors.

2. Methodology

To carry out the DFT calculations, we have used the crystallographic data from Beurmann's work [30] for orthorhombic $SrSnO_3$. The experimental lattice parameters are: a=5.7082(3) Å, b=5.7035(3) Å, and c=8.0659(6) Å, and the space group is *Pbnm* (62), with four chemical formula per unit cell. In a $SrSnO_3$ unit cell, tilted SrO_6 octahedra are intercalated with Sn atoms, as shown in Fig. 1.

To perform the calculations we have used the CASTEP code [31] within the density functional theory (DFT) formalism [32,33]. Two exchange-correlation functionals were taken into account: the total local density approximation (LDA) [33–35] and the generalized gradient approximation [36,37]. The LDA functional uses standard parametrization [38,39], while the GGA functional is the one proposed by Perdew–Burke–Ernzerhof [40]. The PBE functional leads to results close to the ones obtained using the PW91 functional [41]. We have also adopted pseudopotentials to replace the core electrons in each atomic species. For the LDA case, ultrasoft Vanderbilt-type pseudopotentials were used [42], while norm-conserved pseudopotentials [43], generated using the OPIUM code [44], were adopted in the GGA calculations. The electronic valence configurations for each atomic species were: Sr-4$s^2$4$p^6$5s^2, Sn-5$s^2$5p^2, and O-2$s^2$2p^4. A Monkhorst–Pack [45] $4\times4\times3$ sampling was used to evaluate all integrals in reciprocal space, which is more than enough to give a well converged electronic structure.

Lattice parameters and atomic positions were optimized by seeking a total minimum energy for the $SrSnO_3$ unit cell. In order to perform the geometry optimization, the following thresholds were considered for a convergence window of two successive self-consistent steps (except for the GGA-PBE calculations, see the section on the IR-Raman spectra): total energy change smaller than 0.5×10^{-5} eV/atom, maximum force per atom below 0.01 eV/Å, pressure smaller than 0.02 GPa, and maximum atomic displacement not exceeding 0.5×10^{-3} Å. The BFGS minimizer [46] was employed to carry out the unit cell optimization. Within each self-consistent field step, the electronic minimization parameters for convergence were: total energy/atom smaller 0.5×10^{-6} eV, electronic

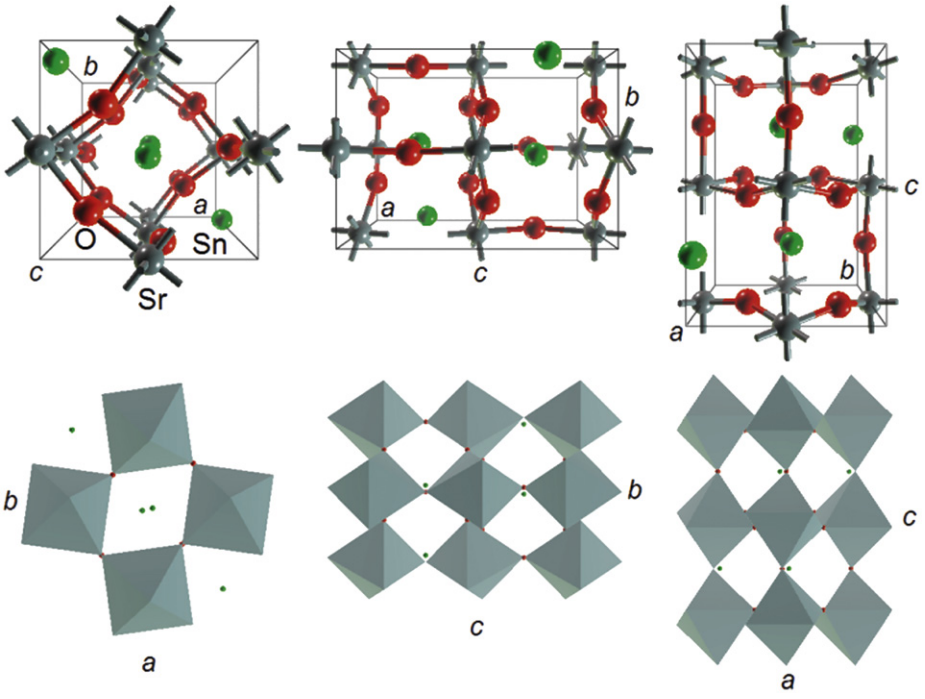

Fig. 1. Crystal structure of $SrSnO_3$ orthorhombic. Top: different views of the unit cell and atomic labels. Bottom: tilted SnO_6 octahedra in the orthorhombic $SrSnO_3$ unit cell.

eigenenergy variation smaller than 0.1471×10^{-6} eV at most, and a convergence window of 3 cycles. A plane-wave basis set was adopted to represent the Kohn–Sham orbitals, with cutoff energy chosen, after convergence studies, to be 500 eV (1000 eV) when using the ultrasoft (norm-conserved) pseudopotentials. The quality of this basis set is kept fixed as the unit cell volume varies during geometry optimization.

After obtaining the unit cell and atomic positions, the Kohn–Sham electronic band structure and the density of states (total and partial, with contributions per atom and per orbital in the last case) were evaluated for both the optimized LDA and GGA unit cells, as well as the complex dielectric function and optical absorption for polarized light. The complex dielectric function $\varepsilon(\omega) = \mathrm{Re}(\varepsilon) + i\mathrm{Im}(\varepsilon)$ and the optical absorption $\alpha(\omega)$ of orthorhombic $SrSnO_3$ were calculated following the same scheme of previous works [15,16,47,48]. Effective masses at the extrema of the valence and conduction bands were estimated by quadratic interpolation of the corresponding band curves [47].

3. Results and discussion

3.1. Volume and geometry optimization

The calculated structural parameters of orthorhombic $SrSnO_3$ are shown in Table 1, together with similar results for orthorhombic $CaSnO_3$ obtained from Ref. [16], for the sake of comparison. Experimental data for $SrSnO_3$ from Beurmann et al. [30] are presented as well. Fractionary atomic coordinates for orthorhombic $SrSnO_3$ are shown in Table 2. LDA lattice parameters are smaller due to the well-known trend of this functional to overestimate the strength of interatomic interactions. For $SrSnO_3$, the difference between LDA and experiment is −1.6% at worst (*c* parameter), while for $CaSnO_3$ the worst difference occurs for the *a* parameter (−1.9%). The GGA exchange-correlation functionals, on the other hand, tend to underestimate the strength of interatomic forces, leading to larger lattice parameters. Notwithstanding that, the GGA estimates for $SrSnO_3$ using norm-conserved pseudopotentials generated by the OPIUM code have the best agreement with X-ray data, with differences between +0.5% (*a* and *c*) and +0.7% (*b*). In comparison, the GGA data for orthorhombic $CaSnO_3$ using ultrasoft pseudopotentials have larger differences in comparison with experiment, even in comparison with the LDA data, being at least +1.7% larger for the *a* parameter. One can note that the $SrSnO_3$ unit cell is larger than the equivalent $CaSnO_3$, which is due to the largest size of the Sr^{2+} ions.

3.2. Band structure, density of states and effective masses

Fig. 2 depicts the full LDA band structure together with the corresponding partial density of states per type of orbital (*s*, *p*, and *d*) contribution. The energy corresponding to 0.0 eV was assigned to the maximum of the valence band (VB) and the number of conduction bands (CBs) calculated was 12. There are deep valence levels in the energy range between −18.0 and −15.5 eV, formed mainly from *s* and *p* orbitals (the latter contribution being much smaller than the former), followed by an energy gap between −15.5 and −14.0 eV and a narrow set of bands between −14.0 and −13.0 eV, formed mainly from *s* and *p* orbitals (the contribution of the *p* orbital being larger than the *s* contribution). A set of dispersive bands between −9.0 and −5.0 eV arises from dominant *s* orbital contributions, followed by another set of bands between −5.0 and 0.0 eV, with dominant contribution from *p* states. The maximum of the valence band occurs at the S point, while the bottom of the conduction band has its minimum clearly visible at Γ. Conduction band curves between 2.3 and 6.3 eV are very dispersive, with contributions from *s* (mainly) and *p* states. Above 6.3 eV, the *p* state contribution becomes dominant and the bands become less dispersive.

Fig. 3 shows a close-up of both the GGA-PBE (dotted) and LDA (solid) Kohn–Sham band structures near the main band gap and the respective total densities of states. These band curves are qualitatively similar for both exchange-correlation functionals. However, the conduction band curves for LDA calculations are about 0.30 eV above the GGA-PBE curves. The valence band maximum, as said before, occurs at the S point in reciprocal space, with a secondary maximum at the Γ point. The conduction band minimum is at the Γ point, with secondary minima located, approximately, at the Z, Y and X points. The smallest band gap is indirect, between the S point in the valence band and the Γ point in the conduction band, being 2.27 eV (1.97 eV) for the LDA (GGA-PBE) functional. Due to the approximations assumed in the construction of the DFT functionals, DFT band gaps are very rough and in general much smaller than experimental data. We can compare the values here obtained with those estimated by Zhang et al. [9], who obtained, using the GGA-RPBE functional, a gap of 1.8 eV (the experimental value reported by these authors is 4.1 eV). For orthorhombic $CaSnO_3$, it was predicted a direct band gap ($\Gamma \rightarrow \Gamma$) with values ranging from 1.95 eV (GGA) to 2.92 eV (LDA) [16].

Fig. 4 depicts the LDA electronic partial density of states (PDOS) for Sr, Sn and O. The most relevant contribution from Sr atoms to the electronic band structure of orthorhombic $SrSnO_3$ is a 4*p* band with maximum at −13.6 eV, and a 4*d* band between 6.0 and 8.5 eV. In comparison, the PDOS for Ca in orthorhombic $CaSnO_3$ has qualitatively the same features, but for different energy ranges: a narrow Ca 3*p* band near −18 eV and a Ca 3*d*

Table 1
Lattice parameters for orthorhombic $SrSnO_3$ according to the DFT-LDA and GGA-PBE approaches. Experimental data for orthorhombic $SrSnO_3$ are also presented [30]. Theoretical and experimental data for orthorhombic $CaSnO_3$ were obtained from Ref. [16]. Lengths *a*,*b*,*c* are in Å and volumes (*V*) in Å^3.

	a	*b*	*c*	*V*
$SrSnO_3$				
LDA	5.621 (−1.5%)	5.637 (−1.2%)	7.943 (−1.6%)	251.702 (−4.2%)
GGA	5.736 (+0.5%)	5.742 (+0.7%)	8.107 (+0.5%)	267.067 (+1.7%)
Exp.	5.7082 (3)	5.7035 (3)	8.0659 (6)	262.600
$CaSnO_3$				
LDA	5.4099 (−1.9%)	5.5887 (−1.4%)	7.7459 (−1.8%)	234.1919 (−4.9%)
GGA	5.6086 (+1.7%)	5.7978 (+2.3%)	8.0452 (+2.1%)	261.6101 (+6.0%)
Exp.	5.5142	5.6634	7.8816	246.1354

Table 2
Internal atomic coordinates for orthorhombic $SrSnO_3$ according with LDA and GGA calculations and experimental values from Ref. [30]. The coordinates (*u*, *v*, *w*) are measured relative to the *a*, *b* and *c* lattice parameters of the unit cell, respectively.

		Internal coordinates		
		u	*v*	*w*
Sr	LDA	−0.006876	0.031750	0.25
	GGA	−0.005262	0.025435	0.25
	Exp.	−0.006(3)	0.023(1)	0.25
Sn	LDA	0	0.5	0
	GGA	0	0.5	0
	Exp.	0	0.5	0
O1	LDA	0.072867	0.483956	0.25
	GGA	0.065496	0.486904	0.25
	Exp.	0.05(2)	0.495(6)	0.25
O2	LDA	0.715134	0.284356	0.038638
	GGA	0.718411	0.281227	0.034440
	Exp.	0.712(7)	0.25(1)	0.033(8)

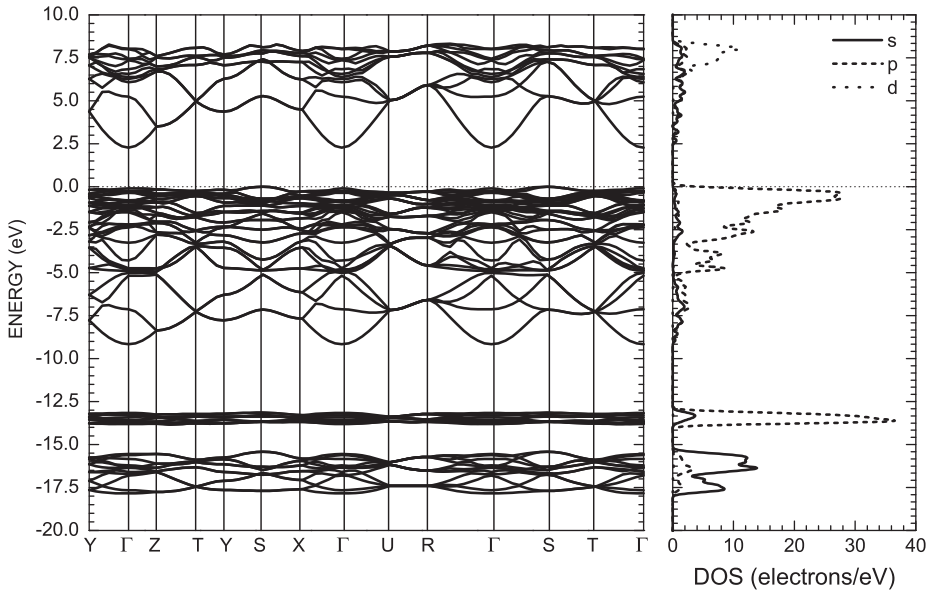

Fig. 2. $SrSnO_3$ orthorhombic Kohn–Sham band structure and partial density of states (PDOS) using the LDA exchange-correlation functional.

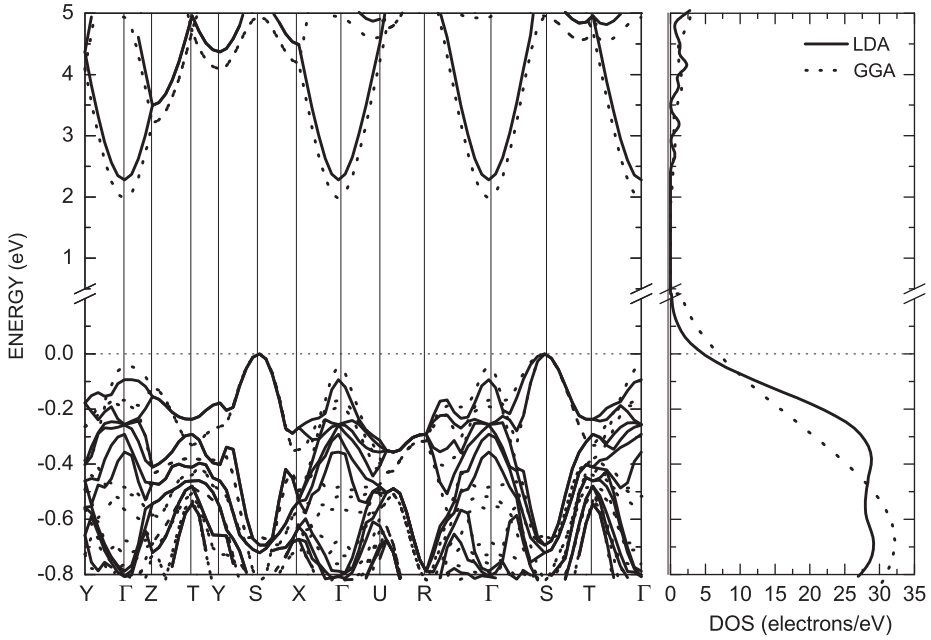

Fig. 3. Electronic band structure for orthorhombic $SrSnO_3$ and partial density of states (PDOS) near the Fermi level (chosen to be zero) calculated using the LDA (solid lines) and GGA-PBE (dotted lines) exchange-correlation functionals.

band between 7 and 11 eV [16]. One may conclude also that the replacement of Ca by Sr reduces the tilting in the structure, turning the Sn 5*s* conduction bands wider and leading to a shift of valence (conduction) bands towards higher (lower) energies, decreasing the band gap of orthorhombic $SrSnO_3$ with respect to orthorhombic $CaSnO_3$ (for these band structure energy shifts, the largest one occurs for the conduction band). The Sn atoms, on the other hand, contribute with three 5*p* DOS bands: the first one between −18.0 and −15.3 eV, the second between −5.0 and 0.0 eV. The third contribution is the most relevant to the formation of the conduction bands between 5.0 and 8.5 eV, in comparison with O and Sr. The 5*s* orbitals originate DOS bands with most pronounced maxima at −17.6, −7.0 (the dispersive bands observed between −9.0 and −5.0 eV, see Fig. 1, are in most part due to Sn 5*s* contributions) and 5.5 eV. The bottom of the conduction band is formed mainly from Sn 5*s* states, leading to the dispersive behavior observed in the LDA band structure shown in Fig. 3. Finally, O 2*p* states are the main contribution to the top of the valence band, in the range −3.0 to 0.0 eV. In the conduction band, however, the O 2*p* levels have small contribution (in comparison with Sn), with 2*p* bands between 5.0 and 6.2 eV, 6.2 and 7.0 eV, and 7.0 and 8.3 eV, respectively. A deep O 2*s* band occurs between −18 and −15 eV. The Sn and O bands observed in orthorhombic $CaSnO_3$ have qualitatively (with energy shifts and variations in band widths) the same pattern of bands described here for orthorhombic $SrSnO_3$ [16].

The semiconducting character of $SrSnO_3$ suggested by the calculated band gaps is reinforced by the effective masses obtained for electrons and holes, shown in Table 3 and found by using a parabolic fit to the non-degenerate valence (conduction) band near its maximum (minimum), using the procedure described in [47]. Hole masses were obtained starting from the

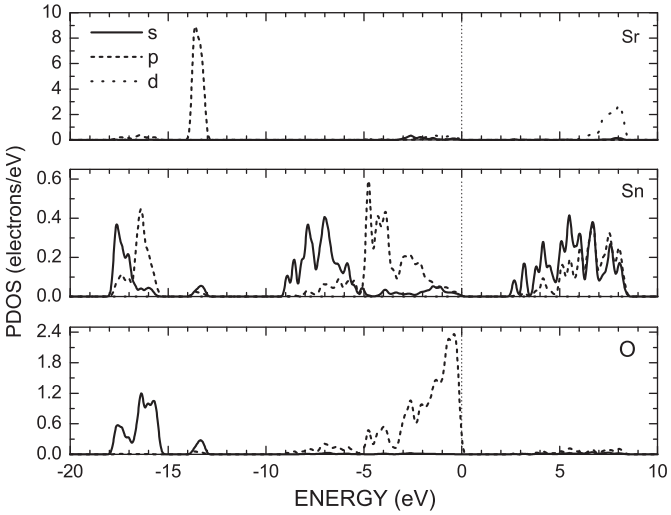

Fig. 4. LDA electronic partial density of states (PDOS) of orthorhombic $SrSnO_3$ per atom (Sr, Sn, O) and per orbital type (s, p, d).

Table 3
Electron and hole effective masses of orthorhombic $SrSnO_3$. All masses are given in terms of the free electron mass (m_0).

Valence band	LDA	GGA	Conduction band	LDA	GGA
$m_h(S\rightarrow Y)$	2.48	2.40	$m_e(\Gamma\rightarrow Y)$	0.46	0.43
$m_h(S\rightarrow X)$	1.04	1.76	$m_e(\Gamma\rightarrow Z)$	0.52	0.92
$m_{lh}(S\rightarrow\Gamma)$	0.78	0.61	$m_e(\Gamma\rightarrow X)$	0.33	0.34
$m_{hh}(S\rightarrow\Gamma)$	1.41	2.14	$m_e(\Gamma\rightarrow U)$	0.26	0.20
$m_h(S\rightarrow T)$	2.75	1.24	$m_e(\Gamma\rightarrow R)$	0.17	0.14
			$m_e(\Gamma\rightarrow S)$	0.21	0.17
			$m_e(\Gamma\rightarrow T)$	0.31	0.24

VB maximum at S along the directions towards the Y, X, Γ and T points. For the S→Γ line, in particular, the existence of two band curves leads to two distinct effective masses, a light hole mass (lh) and a heavy hole mass (hh). LDA and GGA hole masses are very distinct, except for the S→Y and S→Γ directions. In the LDA case, the largest hole mass is observed for the S→T line, being about 2.75 free electron masses (we denote the free electron mass as m_0 from now on), while the heaviest hole in the GGA approximation occurs along the S→Y direction, being 2.40 m_0. The hole with smallest mass is the light hole along S→Γ, being 0.78 m_0 (LDA) and 0.61 m_0 (GGA). Both LDA and GGA calculations predict anisotropic hole masses, and a similar trend is also observed for the electron masses, where LDA and GGA predict similar effective masses along all directions taken into account, except along Γ→Z, where the GGA electron mass is almost twice the LDA value. Indeed, electrons moving along Γ→Z have the largest effective mass in both approaches, being 0.52 m_0 (LDA) and 0.92 m_0 (GGA). The smallest electron effective masses are observed along Γ→R: 0.17 m_0 (LDA) and 0.14 m_0 (GGA). Similar calculations for the hole effective masses in orthorhombic $CaSnO_3$ revealed that this materials also has very anisotropic hole effective masses (with larger mass/smaller mass ratio between 10 and 15, depending on the exchange-correlation functional), but its electron effective masses are very anisotropic, being close to 0.1 m_0 in both the LDA and GGA approaches.

3.3. Optical properties

The real and imaginary parts of the dielectric function $\varepsilon(\omega)=\varepsilon_1(\omega)+i\varepsilon_2(\omega)$ of orthorhombic $SrSnO_3$, calculated within the LDA approach, are shown, respectively, at the top and bottom

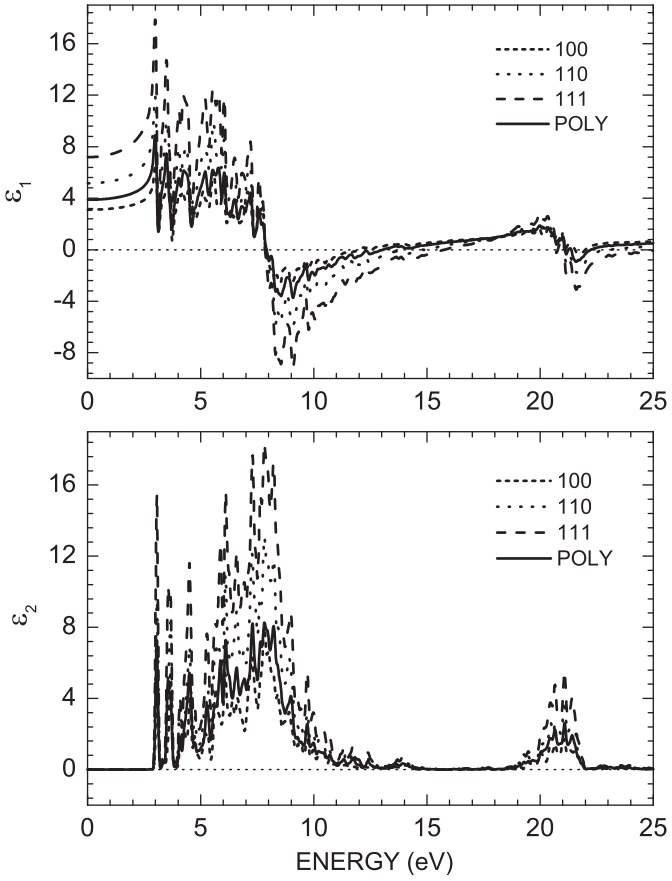

Fig. 5. Real (ε_1) and imaginary (ε_2) parts of the LDA complex dielectric function for orthorhombic $SrSnO_3$. Curves for incident light polarized along distinct crystalline planes (1 0 0, 1 1 0 and 1 1 1) and for light incident on a polycrystalline sample (POLY) are shown.

parts of Fig. 5. Details of the methodology used to obtain $\varepsilon(\omega)$ are given in Ref. [15]. It is also worth to remember that the energy figures in experimental data must be larger than the values presented here due to the well-known underestimation of the energy gap in DFT calculations. Three polarization planes were taken into account for the incident light, coinciding with the [1 0 0], [1 1 0], and [1 1 1] crystalline directions. The case of a polycrystalline (POLY) sample was also considered. Overall, the components of ε are sensitive to the polarization direction. For the real part, ε_1, one can see that the largest overall variation with energy occurs for incident light polarized along [1 1 1], and the smallest variation corresponds to the [1 0 0] polarization case (dielectric function components calculated along [0 1 0] and [0 0 1], not shown in Fig. 5, have curves very similar to the [1 0 0] components). ε_1 also becomes negative in the energy range between 7.6 and 12–15 eV and at about 21 eV. The imaginary part, ε_2, has two bands, the first between 3 eV and about 15 eV, and the second between 19 and 22 eV, with peaks associated with the [1 1 1] polarization more intense in comparison with the [1 1 0] and [1 0 0] cases. For the polycrystalline sample, the maxima and minima of ε_1 and ε_2 are more intense in comparison with the [1 0 0] polarization curve, but less intense than the curves for [1 1 0] and [1 1 1].

The optical absorption curve is closely related to ε_2, being shown in Fig. 6. In it, one can see a set of peaks of similar height at 3.1, 3.6, 4.5, and 5.3 eV. In this energy range, optical absorption varies by a little amount and it is due to electronic transitions from O 2*p* valence bands and Sn 5*s* conduction bands. However, starting from 5.8 eV, optical absorption increases. This change of

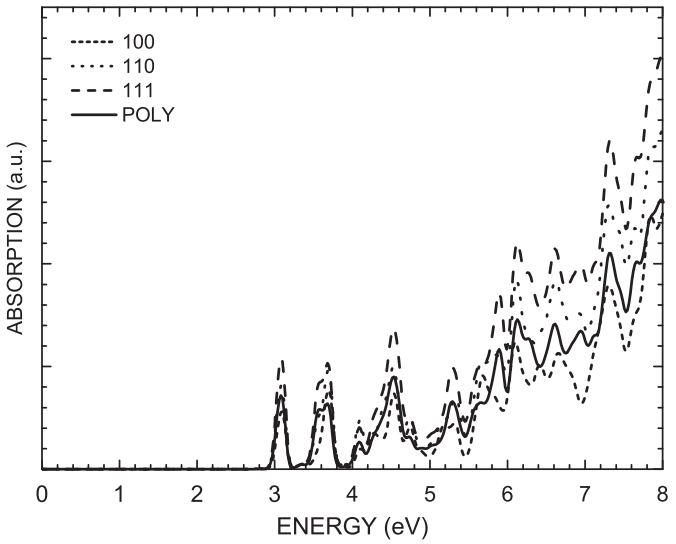

Fig. 6. Optical absorption of orthorhombic $SrSnO_3$ near the main energy band gap when the incident light is polarized along the crystal planes 1 0 0, 1 1 0 and 1 1 1, and for a polycrystalline sample (POLY), using the LDA exchange-correlation functional.

regime is due to the appearance of transitions from the top O 2*p* valence band to a set of Sr 4*d* conduction bands near 6 eV. The same polarization anisotropy observed for the complex dielectric function is also present in the optical absorption, with the [1 0 0] polarized light displaying smaller absorption intensities and the [1 1 1] polarized light having the most intense absorption peaks.

3.4. Infrared and Raman spectra, dielectric permittivities and polarizabilities

In order to obtain the infrared and Raman spectra of orthorhombic $SrSnO_3$ we have used the GGA-PBE exchange-correlation functional. The geometry optimization criteria were more stringent than the ones used for the LDA calculations. The convergence thresholds were: total energy convergence tolerance smaller than 10^{-6} eV/atom, maximum ionic force smaller than 10^{-3} eV/Å, maximum ionic displacement tolerance of 10^{-4} Å and maximum stress component smaller than 0.3×10^{-2} GPa. For the self-consistent field calculations, the convergence criteria took into account a total energy per atom variation smaller than 10^{-7} eV and electronic eigenenergy variation smaller than 0.2381×10^{-7} eV. The linear response scheme was adopted to obtain phonon frequencies at ($\mathbf{q}=0$) [49]. The infrared absorption intensities are related to the dynamical (Hessian) matrix and to the Born effective charges (also known as atomic polarizability tensors, ATP) [49] and can be obtained by calculating the phonons at the Γ point. The Raman spectrum, on the other hand, is widely used to study the vibrational, rotational, and other low-frequency modes in a system, being based on the Raman effect of inelastic scattering of monochromatic light. The interaction of light with atomic vibrations results in the energy of incident photons being shifted up or down, the energy shift being depending on the spacial derivatives of the macroscopic polarization [50]. The infrared and Raman spectra of the orthorhombic $SrSnO_3$ are shown in Fig. 7, top and bottom parts, respectively. Table 4 present the predicted normal modes with the respective irreducible representations and the assignment of IR and Raman active modes.

Orthorhombic $SrSnO_3$ has 57 normal modes at $\mathbf{q}=0$, with 25 infrared active modes, $\Gamma_{IR}=9B_{1u}+7B_{2u}+9B_{3u}$. According with

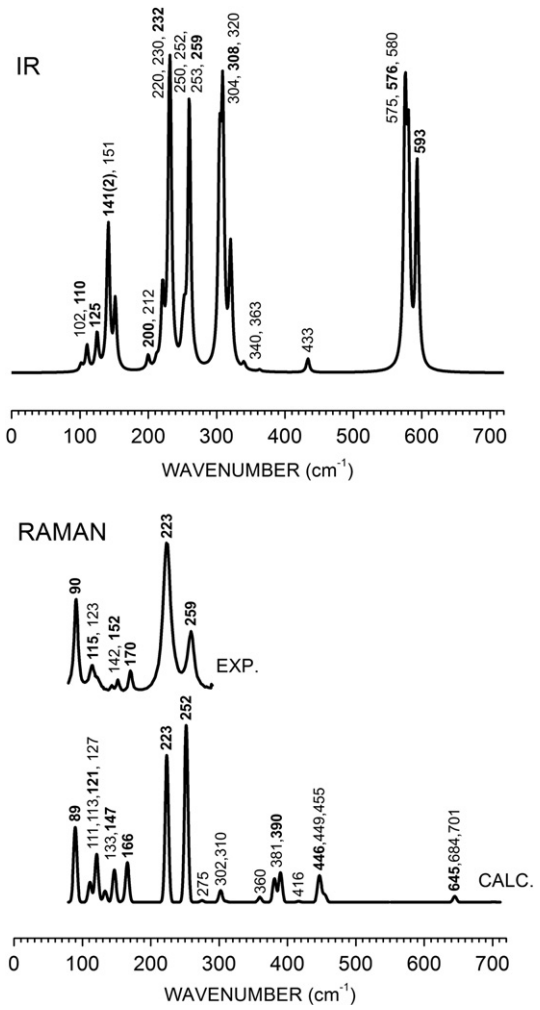

Fig. 7. Infrared (top) and Raman (bottom) spectra of orthorhombic $SrSnO_3$. The numbers correspond to the normal modes shown in Table 4, and bold numbers indicate the most intense peaks. In the Raman spectrum, the inset shows the experimental data of Singh et al. [29] for comparison.

some reports [51,28,52], the vibrations of the stannate group (SnO_3^{2-}) produce high intensity infrared absorption bands in the ranges of 300–400 and 600–700 cm^{-1} [51], with the stretching vibration of the Sn–O bond being located at about 674 cm^{-1} [28] and about 530 cm^{-1} [52]. Looking to the top of Fig. 7, the most intense IR absorption peaks occur at 258.9 cm^{-1} (the band near 230 cm^{-1} looks more intense in comparison, but their individual peaks are less intense than the peak at 258.9 cm^{-1}), a mode with irreducible representation (irrep) B_{3u} which is assigned to a O–Sn–O scissors movement along the *b* axis and a O–Sn–O bending along the *a* axis, within the *ab* plane. The second most intense peak appears at 308.3 cm^{-1} being assigned to a O–Sn–O bending movement in the *ab* plane with irreducible representation B_{2u}, and the third most intense occurs at 575.8 cm^{-1}, corresponding to an assymmetrical Sn–O–Sn stretching with irrep B_{3u}. Two close peaks at 229.9 and 231.6 cm^{-1} produce a very intense absorption band and correspond to a Sn–O–Sn scissoring within the *ab* plane and along the *c* axis, respectively. Smaller peaks can be seen at 141 cm^{-1} (indicated in Fig. 7 as 141(2)), related with the movement of Sr ions up and down (and SnO_6 tetrahedra down and up) along the *c* axis and left and right along the *b* axis (SnO_6 tetrahedra right and left). At 593.1 cm^{-1}, an intense absorption peak is also noted, being assigned to an asymmetrical Sn–O–Sn bond stretching.

Table 4
Normal modes of orthorhombic $SrSnO_3$ at $\mathbf{q}=0$. Irreducible representations (Irreps) are indicated, as well as the IR and Raman active modes.

N	k (cm^{-1})	Irrep	IR	Raman	N	v (cm^{-1})	Irrep	IR	Raman
1	89.5	A_g	N	Y	30	255.7	A_u	N	N
2	97.3	A_u	N	N	31	258.9	B_{3u}	Y	N
3	101.7	B_{1u}	Y	N	32	275.0	B_{3g}	N	Y
4	110.1	B_{3u}	Y	N	33	302.2	B_{1g}	N	Y
5	110.9	A_g	N	Y	34	303.8	B_{1u}	Y	N
6	113.0	B_{2g}	N	Y	35	306.5	A_u	N	N
7	120.8	B_{1g}	N	Y	36	308.3	B_{2u}	Y	N
8	124.7	B_{2u}	Y	N	37	309.6	B_{2g}	N	Y
9	126.9	B_{2g}	N	Y	38	320.1	B_{1u}	Y	N
10	132.2	A_u	N	N	39	339.9	B_{1u}	Y	N
11	133.2	B_{3g}	N	Y	40	359.6	B_{2g}	N	Y
12	141.0	B_{2u}	Y	N	41	362.6	B_{3u}	Y	N
13	141.1	B_{3u}	Y	N	42	381.0	B_{3g}	N	Y
14	146.7	B_{2g}	N	Y	43	389.8	A_g	N	Y
15	151.4	B_{1u}	Y	N	44	416.2	B_{2g}	N	Y
16	154.6	A_u	N	N	45	433.4	B_{3u}	Y	N
17	158.9	B_{3g}	N	Y	46	446.1	B_{3g}	N	Y
18	165.7	A_g	N	Y	47	449.0	B_{3g}	N	Y
19	199.6	B_{3u}	Y	N	48	454.7	A_g	N	Y
20	212.1	B_{1u}	Y	N	49	572.0	A_u	N	N
21	219.5	A_u	N	N	50	574.6	B_{2u}	Y	N
22	220.5	B_{3u}	Y	N	51	575.8	B_{3u}	Y	N
23	223.4	A_g	N	Y	52	580.4	B_{2u}	Y	N
24	229.9	B_{1u}	Y	N	53	586.5	A_u	N	N
25	231.6	B_{2u}	Y	N	54	593.1	B_{1u}	Y	N
26	250.3	B_{2u}	Y	N	55	644.8	B_{3g}	N	Y
27	251.8	A_g	N	Y	56	684.1	B_{2g}	N	Y
28	252.4	B_{3u}	Y	N	57	701.5	B_{3g}	N	Y
29	252.7	B_{1u}	Y	N					

At the bottom of Fig. 7, one can see the calculated Raman scattering spectrum and, as an inset, the experimental curve obtained by Singh et al. [29] for comparison. There is a nice agreement between both the theoretical and experimental curves. There are 24 Raman active modes at $\mathbf{q}=0$ with $\Gamma_{Raman} = 7A_g+5B_{1\,g}+7B_{2\,g}+5B_{3\,g}$. The intense peak at 223 cm^{-1} (both in theory and experiment) is assigned to an A_g mode corresponding to the scissors movement of Sn–O–Sn groups along the c axis, while the peak at 90 cm^{-1} in experiment (89 cm^{-1}, calculated) is due to an A_g mode related with the bending of O–Sn–O groups within the ab plane and the simultaneous movement of Sr ions along the b axis. The peaks at 259 cm^{-1} (exp.) and 252 cm^{-1} (theory, also A_g irrep) are related to O–Sn–O bending within the ab plane and Sn–O–Sn scissoring perpendicular to the c axis. The theoretical Raman curve goes beyond 300 cm^{-1}, and predicts a set of bands near 380 and 450 cm^{-1}, and a band between 640 and 710 cm^{-1}. Finally, there are 8 A_u vibrational modes not detectable by infrared or Raman measurements. The optical permittivity tensor components calculated for orthorhombic $SrSnO_3$ at $\omega=0$ are: $\varepsilon_{xx}=14.787$, $\varepsilon_{yy}=17.704$, $\varepsilon_{zz}=16.102$, $\varepsilon_{xy}=\varepsilon_{xz}=\varepsilon_{yz}=0$. At $\omega=\infty$ we have: $\varepsilon_{xx}=3.838$, $\varepsilon_{yy}=3.797$, $\varepsilon_{zz}=3.807$, $\varepsilon_{xy}=\varepsilon_{xz}=\varepsilon_{yz}=0$. The tensor of polarisabilities (in $Å^3$) for $\omega=0$ (∞) has components: p_{xx}=292.990 (60.311), p_{yy}=354.971(59.436), p_{zz}=320.933 (59.655), $p_{xy}=p_{xz}=p_{yz}=0$ (0).

4. Conclusions

The DFT calculations performed for orthorhombic $SrSnO_3$ predict structural properties very close to experiment when the GGA-PBE exchange-correlation functional is adopted. The maximum difference between the calculated GGA-PBE structure and the experimental data is found for the lattice parameter b, being only +0.7%. LDA figures are good, but not so close, with a difference of −1.6% in the worst case (c length). The electronic band structure reveals that $SrSnO_3$ is an indirect band gap semiconductor, with valence band maximum at the S point and conduction band minimum at the Γ point. The value of the band gap is 2.27 eV (1.97 eV) according with the LDA (GGA-PBE) computations (in comparison, the experimental estimate for the band gap is 4.1 eV). The top of the valence band is formed mainly from O 2p levels, while the bottom of the conduction band arises mainly from Sn 5s electronic states. Analysis of the band curvatures shows that both the hole and electron effective masses at the band extrema are anisotropic, in contrast with $CaSnO_3$, which has very isotropic electron effective masses. Hole masses vary between 0.78 and 2.75 (0.61–2.40) free electron masses within the LDA (GGA-PBE) approach, while electron masses vary between 0.17 and 0.52 (0.14–0.92) free electron masses. These results could be useful when modeling the carrier transport in $SrSnO_3$ films. The complex dielectric function of orthorhombic $SrSnO_3$ is anisotropic with respect to light polarization, with its real and imaginary parts exhibiting more pronounced variation with energy when the polarization plane is aligned with the [111] crystalline direction. The same occurs for the optical absorption. Finally, the infrared and Raman spectra were obtained from the simulations, with the most intense infrared absorption peak near 259 cm^{-1} and the second most intense peak at about 308 cm^{-1}. Another pronounced IR absorption peak appears near 600 cm^{-1}, in the same wavenumber region where high intensity absorption bands are observed experimentally. The calculated Raman spectrum, on the other hand, exhibits a very good agreement with experimental data, with the most intense peak in experiment at 223 cm^{-1} being assigned to an A_g mode corresponding to a scissoring movement of Sn–O–Sn groups along a direction perpendicular to the c axis.

Acknowledgments

ELA, EWSC, and VNF are senior researchers from CNPq, and would like to acknowledge the financial support received during the research development. This work was partially financed by the Brazilian Research Agencies CAPES (Rede NanoBioTec and PROCAD), CNPq (INCT-Nano(Bio)Simes, Project no. 573925/2008-9) and FAPERN/CNPq (Pronex).

References

[1] I. Hamberg, C.G. Granqvist, J. Appl. Phys. 60 (1986) R123.
[2] T. Minami, Semicond. Sci. Technol. 20 (2005) S35.
[3] Y. Furubayashi, T. Hitosugi, Y. Yamamoto, K. Inaba, G. Kinoda, Y. Hirose, T. Shimada, T. Hasegawa, Appl. Phys. Lett. 86 (2005) 252101.
[4] J. Cui, A. Wang, N.L. Edleman, J. Ni, P. Lee, N.R. Armstrong, T.J. Marks, Adv. Mater. 13 (2001) 1476.
[5] H. Kim, C.M. Gilmore, J.S. Horwitz, A. Piqué, H. Murata, G.P. Kushto, R. Schlaf, Z.H. Kafafi, D.B. Chrisey, Appl. Phys. Lett. 76 (2000) 259.
[6] X. Jiang, F.L. Wong, M.K. Fung, S.T. Lee, Appl. Phys. Lett. 83 (2003) 1875.
[7] W. Lu, S. Jiang, D. Zhou, S. Gong, Sensors Actuators 80 (2000) 35.
[8] X.Y. Wie, X. Yao, Mater. Sci. Eng. B 137 (2007) 184.
[9] W.F. Zhang, J. Tang, J. Ye, Chem. Phys. Lett. 418 (2006) 174.
[10] B. Bellal, B. Hadjarab, A. Bouguelia, M. Trari, Theor. and Exp. Chem. 45 (2009) 172.
[11] N. Al-Dahoudi, H. Bisht, C. Göbbert, T. Krajewski, M.A. Aegerter, Thin Solid Films 392 (2001) 299.
[12] H. Mizoguchi, H.W. Eng, P.M. Woodward, Inorg. Chem. 43 (2004) 1667.
[13] Z. Lu, J. Liu, J. Tang, Y. Li, Inorg. Chem. Commun. 7 (2004) 731.
[14] Q.Z. Liu, H.F. Wang, F. Chen, W. Wu, J. Appl. Phys. 103 (2008) 093709.
[15] J.M. Henriques, E.W.S. Caetano, V.N. Freire, J.A.P. da Costa, E.L. Albuquerque, J. Solid State Chem. 180 (2007) 974.
[16] J.M. Henriques, E.W.S. Caetano, V.N. Freire, J.A.P. da Costa, E.L. Albuquerque, J. Phys.: Condens. Matter 19 (2007) 106214.
[17] J.M. Henriques, C.A. Barboza, E.L. Albuquerque, E.W.S. Caetano, V.N. Freire, J.A.P. da Costa, J. Phys. D Appl. Phys. 41 (2008) 065405.
[18] C.A. Barboza, J.M. Henriques, E.L. Albuquerque, E.W.S. Caetano, V.N. Freire, J.A.P. da Costa, Chem. Phys. Lett. 480 (2009) 273.
[19] B. Durand, H. Loiseleur, J. Appl. Cryst. 11 (1978) 289.

[20] E.H. Mountstevens, J.P. Attfield, S.A.T. Redfern, J. Phys.: Condens. Matter 15 (2005) 8315.
[21] H. Mizoguchi, P.M. Woodward, Chem. Mater. 16 (2004) 5233.
[22] I.R. Shein, V.L. Kozhevnikov, A.L. Ivanovkii, Semiconductors 40 (2006) 1261.
[23] V.V. Bannikov, I.R. Shein, V.L. Kozhevnikov, A.L. Ivanovskii, J. Magn. Magn. Mater. 320 (2008) 936.
[24] W. Coffen, J. Am. Ceram. Soc. 36 (1953) 207.
[25] H.D. Megaw, Proc. Phys. Soc. 58 (1946) 133.
[26] A. Vegas, M. Vallet-Regi, J.M. Gonzles-Calbet, M.A. Alario-Franco, Acta Crys. B 42 (1986) 167.
[27] M. Glerup, K.S. Knight, F.W. Poulsen, Mater. Res. Bull. 40 (2005) 507.
[28] M.C.F. Alves, S.C. Souza, M.R.S. Silva, E.C. Paris, S.J.G. Lima, R.M. Gomes, E. Longo, A.G. de Souza, I.M. Garcia dos Santos, J. Therm. Anal. Calorim. 97 (2009) 179.
[29] M.K. Singh, J.W. Hong, N.K. Karan, H.M. Jang, R.S. Katiyar, S.A.T. Redfern, J.F. Scott, J. Phys.: Condens. Matter 22 (2010) 095901.
[30] P.S. Beurmann, V. Thangadurai, W. Weppner, J. Solid State Chem. 174 (2003) 392.
[31] M.D. Segall, P.L.D. Lindan, M.J. Probert, C.J. Pickard, P.J. Hasnip, S.J. Clark, M.C. Payne, J. Phys.: Condens. Matter 14 (2002) 2717.
[32] P. Hohenberg, W. Kohn, Phys. Rev. 136 (1964) B864.
[33] W. Kohn, L.J. Sham, Phys. Rev. 140 (1965) A1133.
[34] R.O. Jones, O. Gunnarsson, Rev. Mod. Phys. 61 (1989) 689.
[35] O.V. Gritsenko, P.R. Schipper, E.J. Baerends, J. Chem. Phys. 107 (1997) 5007.
[36] A. Dal Corso, A. Pasquarello, A. Baldereschi, R. Car, Phys. Rev. B 53 (1996) 1180.
[37] M. Fuchs, M. Bockstedte, E. Pehlke, M. Scheffler, Phys. Rev. B 57 (1998) 2134.
[38] D.M. Ceperley, B.J. Alder, Phys. Rev. Lett. 45 (1980) 566.
[39] J.P. Perdew, A. Zunger, Phys. Rev. B 23 (1981) 5048.
[40] J.P. Perdew, K. Burke, M. Ernzerhof, Phys. Rev. Lett. 77 (1996) 3865.
[41] J.P. Perdew, J.A. Chevary, S.H. Vosko, K.A. Jackson, M.R. Pederson, D.J. Singh, C. Fiolhais, Phys. Rev. B 46 (1992) 6671.
[42] D. Vanderbilt, Phys. Rev. B 41 (1990) 7892.
[43] J.S. Lin, A. Qteish, M.C. Payne, V. Heine, Phys. Rev. B 47 (1993) 4174.
[44] A.M. Rappe, K.M. Rabe, E. Kaxiras, J.D. Joannopoulos, Phys. Rev. B 41 (1990) 1227.
[45] H.J. Monkhorst, J.D. Pack, Phys. Rev. B 13 (1976) 5188.
[46] B.G. Pfrommer, M. Cote, S.G. Louie, M.L. Cohen, J. Comput. Phys. 131 (1997) 133.
[47] J.M. Henriques, E.W.S. Caetano, V.N. Freire, J.A.P. da Costa, E.L. Albuquerque, Chem. Phys. Lett. 427 (2006) 113.
[48] C.A. Barboza, J.M. Henriques, E.L. Albuquerque, V.N. Freire, J.A.P. da Costa, E.W.S. Caetano, J. Phys. D: Appl. Phys. 42 (2009) 155406.
[49] S. Baroni, S. de Gironcoli, A. dal Corso, P. Giannozzi, Rev. Mod. Phys. 73 (2001) 515.
[50] D. Porezag, M.R. Pederson, Phys. Rev. B 54 (1996) 7830.
[51] M. Licheron, G. Jouarf, E. Hussona, J. Eur. Ceram. Soc. 17 (1997) 1453.
[52] R. Nyquist, R. Kagel, Infrared Spectra of Inorganic Compounds, Academic Press, London, 1971.